

Cobalt Incorporated Pyramidal Shaped α -Fe₂O₃ Nanoparticles from Polyvinyl Alcohol Based Precursor

Atanu Naskar¹, Susanta Bera¹, Awadesh Kumar Mallik², Sunirmal Jana^{1*}

¹Sol-Gel Division, CSIR-Central Glass and Ceramic Research Institute (CSIR-CGCRI), P.O. Jadavpur University, Kolkata, India

²Bioceramic and Coating Division, CSIR-Central Glass and Ceramic Research Institute (CSIR-CGCRI), P.O. Jadavpur University, Kolkata, India

Email: *sjana@cgcri.res.in, janasunirmal@hotmail.com

Received 15 December 2015; accepted 3 February 2016; published 6 February 2016

Copyright © 2016 by authors and Scientific Research Publishing Inc.

This work is licensed under the Creative Commons Attribution International License (CC BY).

<http://creativecommons.org/licenses/by/4.0/>



Open Access

Abstract

Precursor foam based Co incorporated α -Fe₂O₃ (AFC) was successfully synthesized at 600°C calcination temperature by simple solution method using PVA. The formation of α -Fe₂O₃ nanoparticles was confirmed by X-ray diffraction measurement and reduction in crystallite size was found after cobalt incorporation. Field emission scanning electron microscopy revealed the existence of pyramidal shaped iron oxide in AFC. FTIR and Raman spectra also confirmed the presence of α -Fe₂O₃. Photocatalytic activity study showed that the cobalt incorporated α -Fe₂O₃ was better photocatalyst than pure α -Fe₂O₃. The cobalt incorporated iron oxide nanoparticles could be used for drug delivery application and this simple preparation method could be adopted for the synthesis of other transition metal oxides.

Keywords

Sol-Gel Based Foam, α -Fe₂O₃ Nanoparticles, Polyvinyl Alcohol, Catalytic Activity

1. Introduction

Nanomaterials (NMs) have received a great deal of interest because of their size dependent amazing properties and versatile applications [1]-[3]. Many methods have been developed for synthesis of NMs [4]-[9]. However, to prepare the nanomaterial from precursor foam, metal salt with an organic binder is generally used [4]. Among the organic binders, polyvinyl alcohol (PVA) can be used as an organic binder [4], because the PVA is com-

*Corresponding author.

pletely removed at relatively lower temperature leaving behind metal oxide mostly in porous form [10]. Moreover, the PVA can reduce the agglomeration problem of nanoparticles. On the other hand, among the NMs, nano iron oxide has attracted much attention due to its application in various fields such as biosensor [11], gas sensor [12], magnetic resonance imaging [13], drug delivery system [14], magnetic devices [15] etc. Iron oxide is mainly found as FeO, Fe₂O₃ and Fe₃O₄ (magnetite) in which Fe₂O₃ has four crystallographic phases, α -Fe₂O₃ (hematite), β -Fe₂O₃, γ -Fe₂O₃ and ϵ -Fe₂O₃ but the hematite (band gap, 2.1 eV) phase is the most stable iron oxide, capable of forming hierarchical microstructures such as hollow fibres [16], rhombohedra [17], cubes [18], rods [19] etc. It is noted that the properties of NMs can be advanced [14] by incorporation of suitable element into nanometal oxide. To the best of our knowledge, no report is yet available in the literature on the synthesis of cobalt incorporated pyramidal shaped hematite in using PVA in the precursor.

Therefore, in the present work, we report cobalt incorporated α -Fe₂O₃ nanoparticles mostly in pyramidal shape by simple solution route from a foam-like precursor having Fe(NO₃)₃·9H₂O and CoCl₂·6H₂O salts as the sources of iron oxide and cobalt, respectively in presence of PVA as an organic binder and in water as solvent respectively. To obtain the final product, the precursor was calcined at 600°C in air atmosphere. The structural property of samples was characterized by X-ray diffraction and field emission scanning electron microscope whereas the spectral properties were measured by using UV-Vis, FTIR and Raman spectral studies. Finally, photocatalytic activity of the samples towards degradation of rhodamine B dye was checked under visible light irradiation.

2. Experiments

2.1. Materials

Ferric nitrate (Fe(NO₃)₃·9H₂O) (Merck, purity 98%), cobaltous chloride (CoCl₂·6H₂O, Merck; purity, ≥98%) as the sources of iron and cobalt, respectively and polyvinyl alcohol (PVA, BDH, molecular weight ~22,000; purity, 98%) as organic binder were purchased and used without their further purifications. Double distilled water was used as a solvent to prepare the precursor solution.

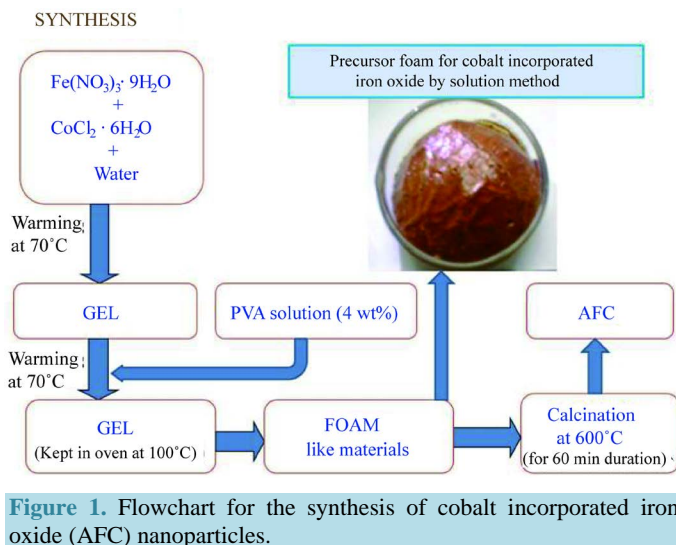
2.2. Synthesis of Pure and Co Incorporated α -Fe₂O₃

Pure and 10% Co incorporated α -Fe₂O₃ were prepared by a simple and cost effective solution method. In this work, the preparation strategy of iron oxide from foam-based precursor is reported for the first time. In a typical synthesis, 2.88 g iron nitrate and 0.19 g cobalt chloride was dissolved (Fe:Co, 90:10; atomic ratio) in double distilled water and heated the solution at 70°C to obtain a gel like material. The gel was formed after 2 h with continuous stirring of the precursor solution. On the other hand, a clear solution containing 4 wt% PVA was made by stirring and warming the solution at 40°C. After that an appropriate amount PVA solution (7 ml) was added slowly to the gel with vigorous stirring. The solution was found to transform into a gel after stirring and warming at 70°C for an hour. The gel was kept at 100°C in an air oven and obtained a foam-like material. In the next, the foam was heat-treated under air atmosphere at 600°C for 60 min to remove the organics and the product of cobalt incorporated α -Fe₂O₃ (AFC) was obtained. Similar procedure was also adopted for preparation of undoped α -Fe₂O₃ (AF) without the addition of hydrated cobaltous chloride in the precursor solution. A flowchart of the overall synthesis process is shown in **Figure 1**. It is worthy to note that the foam formation depends upon the PVA weight percentage (wt%). In this respect, initially the synthesis was made by adding 2 wt% PVA solution but there was no formation of the foam-like material.

3. Characterizations

3.1. Materials Characterization

X-ray diffraction (XRD) study of the samples was performed by X-ray diffractometer (Bruker D8 Advance with DAVINCI design X-ray diffraction unit) with nickel filtered CuK _{α} radiation source ($\lambda = 1.5418 \text{ \AA}$) in the 2θ range, 20° - 80°. Morphological property of the samples were measured by adopting field emission scanning electron microscope (FESEM and FESEM-EDS, ZEISS, SUPRATM 35VP). Raman spectra were recorded using micro-Raman (Renishaw in Via Raman microscope). An argon ion laser with an incident wavelength of 514 nm was used as an excitation source for the Raman measurement. FTIR spectral study was carried out by using Thermo Electron Corporation, USA make FTIR spectrometer (Nicolet 5700). For each experiment, the number



of scans was fixed at 100 (wavenumber resolution, 4 cm⁻¹). A Netzsch STA 409 C/CD thermoanalyzer was used for thermogravimetric analysis (TG-DTA) of the composite using Al₂O₃ as a reference maintaining the heating rate of 10 K/min in air. For the TG-DTA run, a maximum temperature was chosen up to 800°C. The UV-Vis spectra were obtained by UV-Vis-NIR spectrophotometer (UV3600, Shimadzu, Japan) by the diffuse reflectance mode with ISR 3600 attachment.

3.2. Photocatalytic Activity Study

The α -Fe₂O₃ (AF), and Co incorporated α -Fe₂O₃ (AFC) samples were dispersed separately in 50 ml 10⁻⁶ M of aqueous rhodamine B (RhB) solution for measurement of photocatalytic activity of the samples. The suspension was stirred in a dark for 1 h to establish adsorption-desorption equilibrium. The amount of samples in the dye solution was kept fixed (1.0 mg/ml). The photocatalytic activity (PA) of samples under visible light (Philips India make tungsten bulb, 200 Watt) towards the degradation of RhB (10⁻⁶ M solution) was monitored by measuring the concentration change of the RhB dye at ~555 nm. The details of PA measurement under visible light were given in our previous report [20]. During the irradiation process, 5 ml of the suspensions were taken out at different time intervals and measured their UV-Vis absorption spectra. The PA of the samples was analyzed by plotting ln(C₀/C) (dye concentration; C₀, initial and C, remnant) versus irradiation time and the degradation rate constant (considering first order kinetics) for sample was determined from the individual plot.

4. Results and Discussion

4.1. Thermal Analysis

Thermogravimetric and differential thermal analyses (TG-DTA) (Figure 2) were performed on as-prepared Co incorporated precursor foam to determine an appropriate calcination temperature of the foam towards formation of cobalt incorporated iron oxide. In the TG curve of the sample, two steps of weight losses, 13% and 51% with the corresponding peaks at ~185°C (endothermic, very broad) and ~330°C (exothermic, sharp), respectively are observed in the DTA curve. There is also an exothermic peak appeared at ~250°C in DTA curve. The first endothermic peak at ~185°C could be attributed to the removal of water [16] whereas the exothermic peak ~250°C could be ascribed to expulsion of nitrates. However, the main pyrolysis of PVA would happen at ~350°C with the weight loss is about 51%. The curve shows that at 600°C calcination temperature there is no appreciable weight loss took place in the sample. Therefore, we selected the calcination temperature of 600°C of the precursor foam to obtain the oxide materials.

4.2. Structural Property

The crystal phase and crystallite size present in the samples were determined by X-ray diffraction (XRD) study.

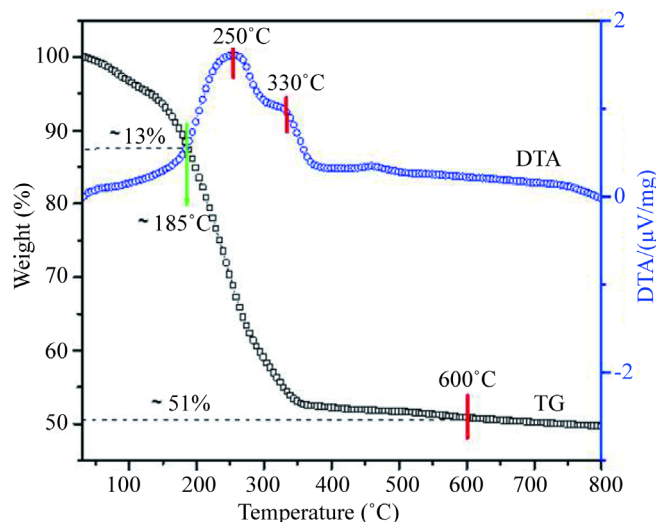


Figure 2. TG and DTA curves of precursor foam for iron oxide.

The XRD patterns of pure iron oxide (AF) as well as cobalt incorporated iron oxide (AFC) samples are shown in **Figure 3**. In both the samples, the XRD peaks (2θ) are observed at 24.1° , 33.1° , 35.6° , 40.8° , 49.4° , 54.1° , 57.5° , 62.4° , 64.1° , 71.9° , and 75.3° that could be indexed to the crystal planes (012), (104), (110), (113), (024), (116), (018), (214), (300), (1010) and (220), respectively of $\alpha\text{-Fe}_2\text{O}_3$ [JCPDS No. 33-0664] [16]. Therefore, cobalt doping is not affecting crystal structure of the iron oxide. Further, no separate phase of metallic cobalt [21] or cobalt oxide crystals [22] was detected in AFC sample. It is worthy to note that the ionic sizes of cobalt ions (Co^{3+}) and iron (Fe^{3+}) ions are approximately similar [23]. Therefore, a considerable amount of dopant could expect to be entered into the Fe_2O_3 crystal lattice [24]. This would be a reason for the non-formation of cobalt/cobalt oxide [25] or its concentration might not be beyond the detection limit by the XRD measurement. The average crystallite size (D) that was estimated by using Debye-Scherrer's equation (Equation (1)) [26] and it was found to be changed in AFC sample. From the XRD patterns, the calculated average crystallite size (± 0.3) of $\alpha\text{-Fe}_2\text{O}_3$ is 15.5 nm and 14.5 nm for AF and AFC, respectively. It is noted that the XRD peak at 2θ , corresponds to (104) plane of iron oxide was used to calculate the average crystallite size. In brief, the XRD analysis confirms that both the samples possess nanocrystalline $\alpha\text{-Fe}_2\text{O}_3$ but the crystallite size of iron oxide is found to reduce slightly in AFC. This result would indicate that the Co would enter into the host lattice [27]. However, the size of the crystallites remained within the nano regime.

$$D = k\lambda/\beta \cos \theta \quad (1)$$

where k is proportionality constant (~ 0.9), λ is wavelength of X-ray (1.5406 \AA), β is FWHM (full width at half maximum) for maximum intensity peak in radians, θ is diffraction angle and D is the crystallite size.

FESEM images of AF and AFC are shown in **Figure 4**. No definite feature of iron oxide (**Figure 4(a)**) was observed in AF whereas the morphology of iron oxide nanoparticles ($0.5 - 1.0 \mu\text{m}$) in cobalt incorporated sample (AFC) was mostly in pyramidal shape (inset i, **Figure 4(b)**).

4.3. FTIR Analysis

FTIR analysis of pure $\alpha\text{-Fe}_2\text{O}_3$ (AF) and Co incorporated $\alpha\text{-Fe}_2\text{O}_3$ (AFC) was done in the spectral range, $4000 - 400 \text{ cm}^{-1}$ (**Figure 5**) to reveal the presence of Fe-O bond vibration and to confirm the absence of organics (PVA) in the calcined samples. The FTIR peaks appeared at 460 cm^{-1} and 580 cm^{-1} in AF and AFC samples could be assigned to Fe-O stretching vibration [28]. This observation supports the XRD result (**Figure 3**). It is worthy to mention that a Co-O stretching vibration peak might be overlapped within the 580 cm^{-1} FTIR peak of Fe-O. A broad peak at 3432 cm^{-1} and also the existence of absorption band in the range of $1670 - 1600 \text{ cm}^{-1}$ [29] would indicate the presence of -OH groups that would present on iron oxide surface. It is important to note that after curing the samples at 600°C for 1 h, the organic materials from PVA decomposition [30] completely removed and formed $\alpha\text{-Fe}_2\text{O}_3$ as observed from TG-DTA study (**Figure 2**).

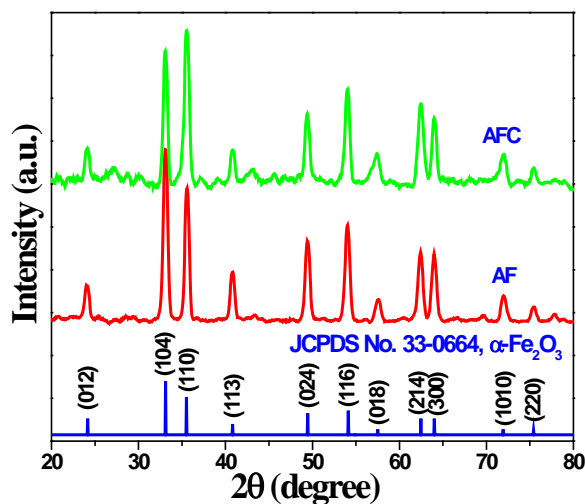


Figure 3. XRD patterns of AF and AFC cured at 600°C.

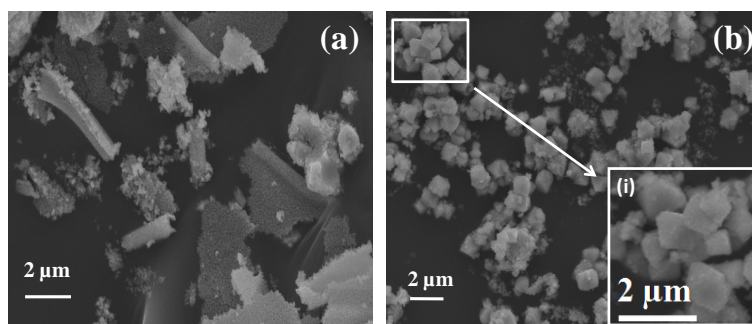


Figure 4. FESEM images of (a) AF and (b) AFC samples.

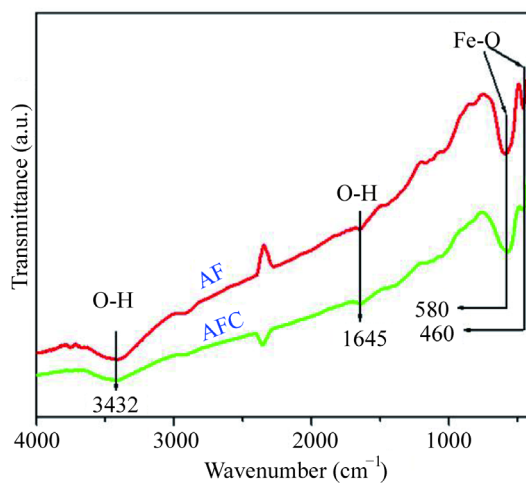


Figure 5. FTIR spectra of AF and AFC samples.

4.4. UV-Visible Spectra

UV-visible spectra of the samples, measured by diffused reflectance spectroscopy are shown in **Figure 6**. Generally, the band edge absorption of α -Fe₂O₃ could be observed in the wavelength range of 520 - 565 nm [31]. The AF sample shows a strong absorption at 530 nm (2.34 eV, would correspond to band gap energy, 2.2 eV of α -Fe₂O₃). This result would also indicate the formation of α -Fe₂O₃ nanoparticles [31]. However, in AFC sample,

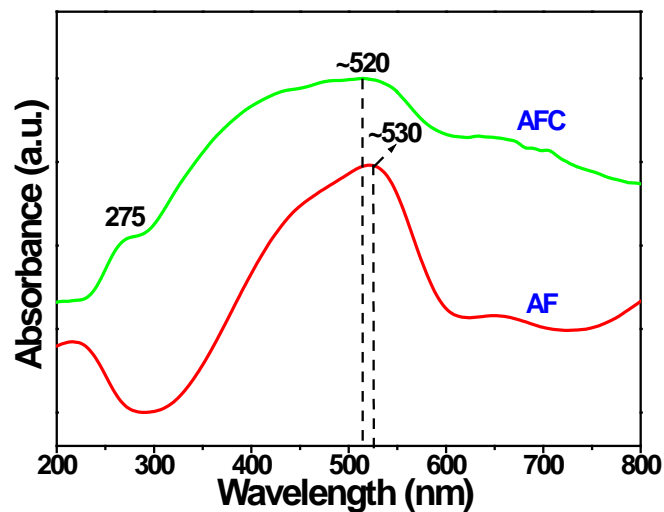


Figure 6. UV-visible absorption spectra of AF and AFC measured by diffuse reflectance method.

the absorption peak is found to shift slightly in the blue wavelength region (520 nm, ~ 2.4 eV). The decrease of crystallite size in the cobalt incorporated iron oxide as measured from XRD study (Figure 3) would be the reason for the peak shifting. The possible reason for the spectral broad in the region 400 - 500 nm in AFC sample would be due to the formation of very low content of cobalt oxide that would remain on the surface of iron oxide nanoparticles. This statement could be justified from the observation of a prominent absorption peak at ~ 275 nm due to Co_3O_4 [22].

4.5. Raman Spectra

Micro-Raman spectral study (Figure 7) of AF and AFC samples was performed to investigate the presence of $\alpha\text{-Fe}_2\text{O}_3$ as well as their relative change of structural defects in the crystals [32].

The Raman peaks appeared at 229, 294, and 413 cm^{-1} , could be assigned to A_{1g} mode (229 cm^{-1}) and E_g mode (294 and 413 cm^{-1}) [31] of $\alpha\text{-Fe}_2\text{O}_3$. This result also confirms the presence of $\alpha\text{-Fe}_2\text{O}_3$ phase and strongly supports the XRD (Figure 3), FTIR (Figure 5) and UV-Vis (Figure 6) spectral results.

4.6. Photocatalytic Activity

Photocatalytic activity (PA) of samples towards degradation of RhB under visible light irradiation was investigated after adsorption-desorption process in the dark environment. Time dependent absorption spectra (remnant dye concentration vs. irradiation time) of aqueous RhB dye solution using AF and AFC as photocatalysts are shown in Figure 8(a). In this experiment, C_0 and C are the initial concentration after adsorption-desorption equilibrium in the dark and actual concentration of RhB dye solution at different irradiation time, respectively. As shown in Figure 8(a), AFC sample showed higher photocatalytic activity compared to AF. The photocatalytic efficiency of the materials was evaluated by calculation of pseudo first order reaction rate constant based with the help of Equation (2).

$$\ln(C_0/C) = kt \quad (2)$$

where, k is the reaction constant and t is the time.

The calculated degradation rate constants, k ($\times 10^{-3} \text{ min}^{-1}$) of AF and AFC samples were found to be 2.5 and 5.3 (Figure 8(b)), respectively. Therefore, the maximum k value was obtained in AFC. Generally, particle size (inversely related to band gap energy) and surface area (inversely proportional to particle size), shape of particles etc. would control the photocatalytic activity of metal oxide semiconductor [33]. In this work, the lower particle size due to cobalt doping and pyramidal shaped of iron oxide in AFC could be considered the favourable factors for the enhancement of PA.

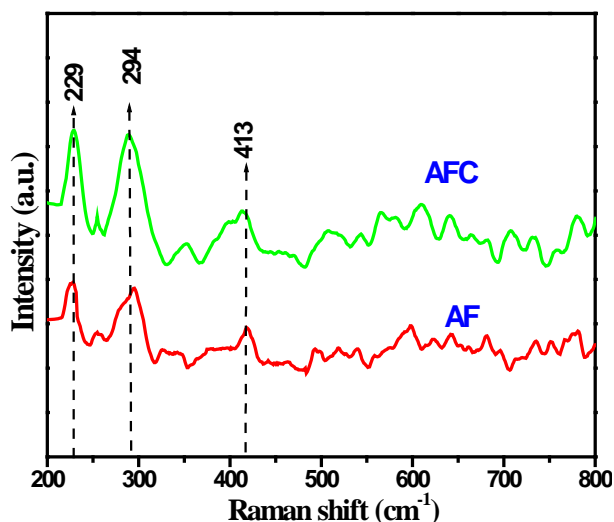


Figure 7. Raman spectra of AF and AFC.

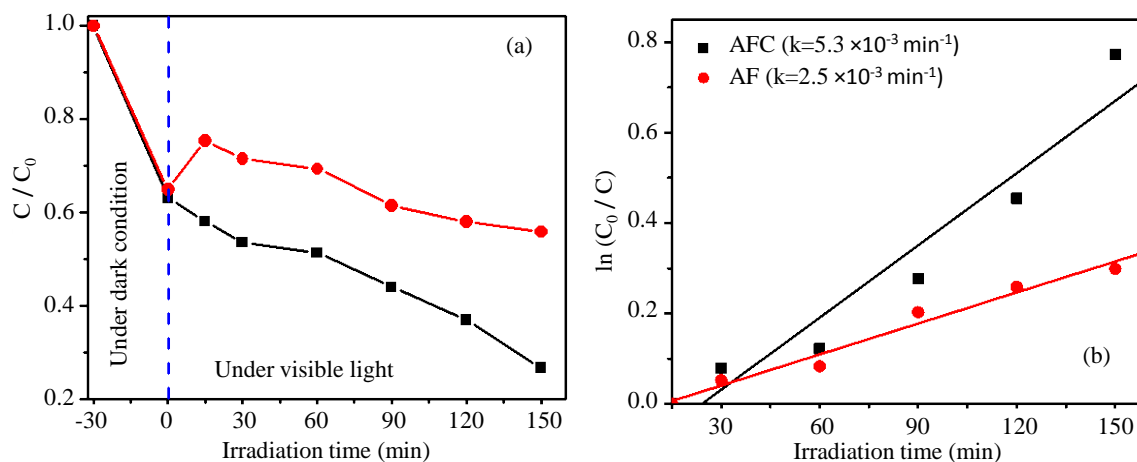


Figure 8. (a) Photocatalytic degradation (remnant dye concentration versus irradiation time) of aqueous RhB dye solution in presence of AF and AFC as photocatalysts; (b) First-order plot for the degradation of RhB under visible light using AF and AFC samples. The rate constants for the dye degradation reaction are embedded in the figure.

5. Conclusion

Nanocrystalline pure and Co incorporated α -Fe₂O₃ (AFC) were successfully synthesized at 600°C calcination temperature from precursor foam by simple solution method using PVA as gelling and stabilizing agent. The formation of α -Fe₂O₃ nanoparticles was confirmed by XRD measurement and reduction in crystallite size was found after cobalt incorporation. Field emission scanning electron microscopy revealed the existence of pyramidal shaped iron oxide in AFC. FTIR and Raman spectra also confirmed the presence of α -Fe₂O₃. Photocatalytic activity study showed that the cobalt incorporated α -Fe₂O₃ was better photocatalyst than pure α -Fe₂O₃. The cobalt incorporated iron oxide nanoparticles could be used for drug delivery application and this simple method could be adopted for synthesis of other transition metal oxides.

Acknowledgements

Authors are grateful to the Director, CSIR-CGRI, Kolkata for his kind support and encouragement for this work. The authors AN and SB thankfully acknowledge UGC-RGNF and CSIR, respectively, Govt. of India for providing their Ph.D. research fellowships. The authors also acknowledge the help rendered by Materials Characterization Division for several measurements of the samples. The work has been done as an associated re-

search work of 12th Five Year Plan project of CSIR (No. ESC0202).

References

- [1] Ramrakhiani, M. (2012) Nanostructures and Their Applications. *Recent Research in Science and Technology*, **4**, 14-19. <http://recent-science.com>
- [2] Kruis, F.E., Fissan, H. and Peled, A. (1998) Synthesis of Nanoparticles in the Gas Phase for Electronic, Optical and Magnetic Applications—A Review. *Journal of Aerosol Science*, **29**, 511-535. [http://dx.doi.org/10.1016/S0021-8502\(97\)10032-5](http://dx.doi.org/10.1016/S0021-8502(97)10032-5)
- [3] Lu, A-H. and Schüth, F. (2006) Nanocasting: A Versatile Strategy for Creating Nanostructured Porous Materials. *Advanced Materials*, **18**, 1793-1805. <http://dx.doi.org/10.1002/adma.200600148>
- [4] Venugopal, B.R., Samuel, E.P., Shivakumara, C. and Rajamathi, M. (2009) Macroporous Metal Oxide Foams through Self-Sustained Combustion Reactions. *Journal of Porous Materials*, **16**, 205-208. <http://dx.doi.org/10.1007/s10934-008-9186-y>
- [5] Ji, X., Tang, S., Gu, L., Liu, T. and Zhang, X. (2015) Synthesis of Rod-Like Mesoporous γ -Al₂O₃ by an Ionic Liquid-Assisted Sol-Gel Method. *Materials Letters*, **151**, 20-23. <http://dx.doi.org/10.1016/j.matlet.2015.03.022>
- [6] Bijanzad, K., Tadjarodi, A. and Akhavan, O. (2015) Photocatalytic Activity of Mesoporous Microbricks of ZnO Nanoparticles Prepared by the Thermal Decomposition of Bis(2-aminonicotinato) Zinc (II). *Chinese Journal of Catalysis*, **36**, 742-749. [http://dx.doi.org/10.1016/S1872-2067\(14\)60305-3](http://dx.doi.org/10.1016/S1872-2067(14)60305-3)
- [7] Ye, X., Xiao, X., Zheng, C., Hua, N. and Huang, Y. (2015) Microemulsion-Assisted Hydrothermal Synthesis of Mesoporous Silver/Titania Composites with Enhanced Infrared Radiation Performance. *Materials Letters*, **152**, 237-239. <http://dx.doi.org/10.1016/j.matlet.2015.03.134>
- [8] Rao, B.N., Kumar, P.R., Padmaraj, O., Venkateswarlu, M. and Satyanarayana, N. (2015) Rapid Microwave Assisted Hydrothermal Synthesis of Porous α -Fe₂O₃ Nanostructures as Stable and High Capacity Negative Electrode for Lithium and Sodium Ion Batteries. *RSC Advances*, **5**, 34761-34768. <http://dx.doi.org/10.1039/C5RA03238E>
- [9] Sundar, S. and Piraman, S. (2013) Nanospheres of Fe₃O₄ Synthesis through Sol Gel Technique and Their Structural & Magnetic Characterization. *Indian Journal of Applied Research*, **3**, 123-126. <http://dx.doi.org/10.15373/2249555X/JULY2013/33>
- [10] Bepari, R.A., Bharali, P. and Das, B.K. (2014) Controlled Synthesis of α - and γ -Fe₂O₃ Nanoparticles via Thermolysis of PVA Gels and Studies on α -Fe₂O₃ Catalyzed Styrene Epoxidation. *Journal of Saudi Chemical Society*, Online. <http://dx.doi.org/10.1016/j.jscs.2013.12.010>
- [11] Tiwari, I., Singh, M., Pandey, C.M. and Sumana, G. (2015) Electrochemical Genosensor Based on Grapheme Oxide Modified Iron Oxide-Chitosan Hybrid Nanocomposite for Pathogen Detection. *Sensors and Actuators B: Chemical*, **206**, 276-283. <http://dx.doi.org/10.1016/j.snb.2014.09.056>
- [12] Cuong, N.D., Khieu, D.Q., Hoa, T.T., Quang, D.T., Viet, P.H., Lam, T.D., Hoa, N.D. and Hieu N.V. (2015) Facile Synthesis of α -Fe₂O₃ Nanoparticles for High-Performance CO Gas Sensor. *Materials Research Bulletin*, **68**, 302-307. <http://dx.doi.org/10.1016/j.materresbull.2015.03.069>
- [13] Verma, V.K., Kamaraju, S.R., Kancherla, R., Kona, L.K., Beevi, S.S., Debnath, T., Usha, S.P., Vadapalli, R., Arbab, A.S. and Chelluri, L.K. (2015) Fluorescent Magnetic Iron Oxide Nanoparticles for Cardiac Precursor Cell Selection from Stromal Vascular Fraction and Optimization for Magnetic Resonance Imaging. *International Journal of Nanomedicine*, **10**, 711-726.
- [14] Hola, K., Markova, Z., Zoppellaro, G., Tucek, J. and Zboril, R. (2015) Tailored Functionalization of Iron Oxide Nanoparticles for MRI, Drug Delivery, Magnetic Separation and Immobilization of Biosubstances. *Biotechnology Advances*, **33**, 1162-1176.
- [15] Saari, M.M., Sakai, K., Kiwa, T., Sasayama, T., Yoshida, T. and Tsukada, K. (2015) Characterization of the Magnetic Moment Distribution in Low-Concentration Solutions of Iron Oxide Nanoparticles by a High-T_c Superconducting Quantum Interference Device Magnetometer. *Journal of Applied Physics*, **117**, Article ID: 17B321.
- [16] Gao, Q., Luo, J., Wang, X., Gao, C. and Ge, M. (2015) Novel Hollow α -Fe₂O₃ Nanofibers via Electrospinning for Dye Adsorption. *Nanoscale Research Letters*, **10**, 176. <http://dx.doi.org/10.1186/s11671-015-0874-7>
- [17] Ávila, C.F., Lagoeiro, L., Barbosa, P.F. and Graca, L. (2015) EBSD Analysis of Rhombohedral Twinning in Hematite Crystals of Naturally Deformed Iron Formations. *Journal of Applied Crystallography*, **48**, 212-219. <http://dx.doi.org/10.1107/S1600576714025928>
- [18] Liu, K., Wang, H., Wu, Q., Zhao, J., Sun, Z. and Xue, S. (2015) Nanocube-Based Hematite Photoanode Produced in the Presence of Na₂HPO₄ for Efficient Solar Water Splitting. *Journal of Power Sources*, **283**, 381-388. <http://dx.doi.org/10.1016/j.jpowsour.2015.02.144>

- [19] Wang, D., Zhang, Y., Peng, C., Wang, J., Huang, Q., Su, S., Wang, L., Huang, W. and Fan, C. (2015) Crystallinity Engineering of Hematite Nanorods for High-Efficiency Photoelectrochemical Water Splitting. *Advance Science*, **2**. <http://dx.doi.org/10.1002/adv.201500005>
- [20] Pal, M., Bera, S., Sarkar, S. and Jana, S. (2014) Influence of Al Doping on Microstructural, Optical and Photocatalytic Properties of Sol-Gel Based Nanostructured Zinc Oxide Films on Glass. *RSC Advances*, **4**, 11552-11563. <http://dx.doi.org/10.1039/c3ra44612c>
- [21] Vasundhara, K., Mandal, B.P. and Tyagi, A.K. (2015) Enhancement of Dielectric Permittivity and Ferroelectricity of a Modified Cobalt Nanoparticle and Polyvinylidene Fluoride Based Composite. *RSC Advances*, **5**, 8591-8597. <http://dx.doi.org/10.1039/C4RA09292A>
- [22] Farhadi, S., Safabakhsh, J. and Zaringhadam, P. (2013) Synthesis, Characterization, and Investigation of Optical and Magnetic Properties of Cobalt Oxide (Co₃O₄) Nanoparticles. *Journal of Nanostructure in Chemistry*, **3**, 69.
- [23] Mamatha, C., Subhashini, P. and Krishnaiah, M. (2015) Effect of Cobalt Substitution on Electrical Properties of Calcium Hexaferrites Nano Particles. *Archives of Applied Science Research*, **7**, 7-11.
- [24] Hou, Y., Zuo, F., Dagg, A. and Feng, P. (2013) A Three-Dimensional Branched Cobalt-Doped α -Fe₂O₃ Nanorod/MgFe₂O₄ Heterojunction Array as a Flexible Photoanode for Efficient Photoelectrochemical Water Oxidation. *Angewandte Chemie International Edition*, **52**, 1248-1252. <http://dx.doi.org/10.1002/anie.201207578>
- [25] Hummelgård, C., Karlsson, R.K.B., Bäckström, J., Rahman, S.M.H., Cornell, A., Eriksson, S. and Olin, H. (2013) Physical and Electrochemical Properties of Cobalt Doped (Ti,Ru)O₂ Electrode Coatings. *Materials Science and Engineering: B*, **178**, 1515-1522. <http://dx.doi.org/10.1016/j.mseb.2013.08.018>
- [26] Patterson, A.L. (1939) The Scherrer Formula for X-Ray Particle Size Determination. *Physical Review*, **56**, 978-982. <http://dx.doi.org/10.1103/PhysRev.56.978>
- [27] Ruikar, D.V., Kashid, P.B., Supugade, S., Pisal, N., Puri, V. (2013) Structural, Electrical and Magnetic Properties of SrCo_xFe_{12-x}O₁₉ (0 ≤ x ≤ 1) Prepared by Co-Precipitation Method. *Advances in Ceramic Science and Engineering*, **2**, 72-77.
- [28] Chernyshova, I.V., Hochella Jr., M.F. and Madden, A.S. (2007) Size-Dependent Structural Transformations of Hematite Nanoparticles. 1. Phase Transition. *Physical Chemistry Chemical Physics*, **9**, 1736-1750. <http://dx.doi.org/10.1039/b618790k>
- [29] Qin, X., Liu, F., Wang, G. and Huang, G. (2015) Adsorption of Humic Acid from Aqueous Solution by Hematite: Effects of pH and Ionic Strength. *Environmental Earth Science*, **73**, 4011-4017. <http://dx.doi.org/10.1007/s12665-014-3686-7>
- [30] Mansur, H.S., Sadahira, C.M., Souza, A.N. and Mansur, A.A.P. (2008) FTIR Spectroscopy Characterization of Poly(vinyl alcohol) Hydrogel with Different Hydrolysis Degree and Chemically Crosslinked with Glutaraldehyde. *Materials Science and Engineering: C*, **28**, 539-548. <http://dx.doi.org/10.1016/j.msec.2007.10.088>
- [31] Oliveira, H.S., Almeida, L.D., de Freitas, V.A.A., Moura, F.C.C., Souza, P.P. and Oliveira, L.C.A. (2015) Nb-Doped Hematite: Highly Active Catalyst for the Oxidation of Organic Dyes in Water. *Catalysis Today*, **240**, 176-181. <http://dx.doi.org/10.1016/j.cattod.2014.07.016>
- [32] Phu, N.D., Ngo, D.T., Hoang, L.H., Luong, N.H. and Hai, N.H. (2011) Crystallization Process and Magnetic Properties of Amorphous Iron Oxide Nanoparticles. *Journal of Physics D: Applied Physics*, **44**, Article ID: 345002. <http://dx.doi.org/10.1088/0022-3727/44/34/345002>
- [33] Pal, M. and Jana, S. (2013) Effect of Precursor Sol pH on Microstructural, Optical and Photocatalytic Properties of Vacuum Annealed Zinc Tin Oxide Thin Films on Glass. *Journal of Sol-Gel Science and Technology*, **67**, 8-17. <http://dx.doi.org/10.1007/s10971-013-3045-2>